Optical flow for particle images with optimization based on a priori knowledge of the flow

Théo Benkovic, Jean-François Krawczynski, Philippe Druault

▶ To cite this version:

Théo Benkovic, Jean-François Krawczynski, Philippe Druault. Optical flow for particle images with optimization based on a priori knowledge of the flow. Measurement Science and Technology, 2023, 34 (10), pp.105301. ⟨10.1088/1361-6501/ace074⟩. ⟨hal-04146637⟩

HAL Id: hal-04146637

https://hal.science/hal-04146637v1

Submitted on 30 Jun 2023

Measurement Science and
Technology

ACCEPTED MANUSCRIPT

Optical flow for particle images with optimization based on a priori knowledge of the flow

To cite this article before publication: Théo Benkovic *et al* 2023 *Meas. Sci. Technol.* in press https://doi.org/10.1088/1361-6501/ace074

Manuscript version: Accepted Manuscript

Accepted Manuscript is “the version of the article accepted for publication including all changes made as a result of the peer review process, and which may also include the addition to the article by IOP Publishing of a header, an article ID, a cover sheet and/or an ‘Accepted Manuscript’ watermark, but excluding any other editing, typesetting or other changes made by IOP Publishing and/or its licensors”

This Accepted Manuscript is **© 2023 IOP Publishing Ltd**.

During the embargo period (the 12 month period from the publication of the Version of Record of this article), the Accepted Manuscript is fully protected by copyright and cannot be reused or reposted elsewhere.

As the Version of Record of this article is going to be / has been published on a subscription basis, this Accepted Manuscript will be available for reuse under a CC BY-NC-ND 3.0 licence after the 12 month embargo period.

After the embargo period, everyone is permitted to use copy and redistribute this article for non-commercial purposes only, provided that they adhere to all the terms of the licence https://creativecommons.org/licences/by-nc-nd/3.0

Although reasonable endeavours have been taken to obtain all necessary permissions from third parties to include their copyrighted content within this article, their full citation and copyright line may not be present in this Accepted Manuscript version. Before using any content from this article, please refer to the Version of Record on IOPscience once published for full citation and copyright details, as permissions may be required. All third party content is fully copyright protected, unless specifically stated otherwise in the figure caption in the Version of Record.

View the article online for updates and enhancements.

This content was downloaded from IP address 134.157.34.205 on 22/06/2023 at 08:21

Optical flow for particle images with optimization based on *a priori* knowledge of the flow

Théo Benkovic, Jean-François Krawczynski & Philippe Druault
Sorbonne Université, CNRS, Institut Jean Le Rond d'Alembert, F-75005 Paris, France
E-mail: `jean-francois.krawczynski@sorbonne-universite.fr`

19 June 2023

Abstract.
This paper proposes a new Optical Flow method for particle image velocimetry applications. The proposed method is based on the use of an *a priori* sparse knowledge of the flow. A particular insight is given to the optimization derivation based on an image-independent method. Two alternatives are introduced. The first one uses particle-tracking velocimetry (PTV) estimates as subpixel information to describe the finest velocity scales. The expected true displacements related to the motion of the individual particles are used as anchors for the optimization procedure when the density of the particles is large enough. Alternatively, the second method solves the well-known median problem based on new image-independent functions in areas of low particle density. Studies have been carried out on synthetic images to characterize the error and analyze the impact of image parameters (particle density, particle size, or noise) on the methods. The new methods are compared with a reference method against synthetic data: two Lamb-Oseen vortex rings and a 3D Turbulent Homogeneous and Isotropic flow. The results show that the performances of the new method exceed those of the reference method in almost all tested cases, except for images with particles of relatively small size. It is notably shown that the new method is less dependent on the particle density and the noise embedded in the images than other optical flow estimators.

Keywords: optical flow, particle tracking velocity (PTV), turbulent flow, optimization, velocity measurements

Submitted to: *Meas. Sci. Technol.*

1. Introduction

The Optical Flow (OF) is the apparent motion of individual pixel brightness between consecutive images. Since the original work of Horn and Schunck in 1981 (Horn and Schunck 1981), its formulation has not changed much. One has to minimize a term defined from the brightness constancy assumption, with a spatial and independent constraint for each velocity component: it is the so-called aperture problem, which is the first-order form of Tikhonov's formulation for ill-posed problems (Tikhonov *et al* 1977). In the meantime, mathematical conditions on the constraint were formulated and their validity was proven (Schnörr 1991), the convergence of these methods was settled at the end of the 1990s (Aubert *et al* 1999) and the physics foundations of the aperture problem were described (Liu and Shen 2008). With these strong mathematical foundations, the fluid mechanics community adapted these methods to velocity measurements using particle images.

The original spatial constraint for the resolution of the aperture problem was a Laplacian null condition for each velocity component. This is a convenient choice as it results in independent constraints for each component, and it is easily computable or discretizable. However, this condition is usually not valid for fluid flows as it tends to minimize both the divergence and the vorticity (Chen *et al* 2015). Moreover, it has been proven that the brightness constancy condition implicitly uses the hypothesis that the flow is divergence-free (Corpetti *et al* 2002). Therefore, many works have been done in the pursuit of a physics-based spatial constraint dedicated to fluid flows. Recently, the implementation of an adaptive Lagrange coefficient was investigated (Schuster *et al* 2018) to balance the relative weight between the brightness constancy equation and the spatial constraint imposed on the velocity field at any iteration. Physics-based constraints, by imposing either a divergence null constraint (Kadri-Harouna *et al* 2013) or the shape of the kinetic energy spectrum (Schmidt and Sutton 2019), were proposed using wavelet formulation to reach a velocity field estimate that follows an *a priori* knowledge of the flow. The search for a constraint-based on physical considerations also led the fluid mechanics community to develop a correction to the OF estimate based on *a priori* knowledge of the flow. To this end, deep learning methods were developed and trained on synthetic images to correct OF estimates from experimental images (Cai *et al* 2019). Estimates from other optical methods, such as Particle Image Velocimetry (PIV) (Heitz *et al* 2008) or Particle Tracking Velocimetry (PTV) (Schneiders and Scarano 2016) were also utilized to constrain or correct the velocity field obtained on a regular grid. Consequently, the large majority of OF studies dedicated to fluid flows ended in spatial constraints or post-correction completely image independent. Some reasons could be advanced.

First, an *a priori* knowledge of the flow is not difficult to obtain, whether it be theoretically, from simulations, or from other optical methods such as PIV.

Second, the particle images are not flawless. Without even talking about purely measurement considerations, particle images are known to contain inherent errors

(Harris *et al* 2012). Taking a shot of a seeded flow with a camera is equivalent to discretizing a continuous signal on pixels, i.e., on a coarse-grained grid. The number and size of the pixels could be insufficient to describe the complexity of the signal, leading to the so-called "pixel-locking" or "peak locking". This error is thoroughly studied for PIV applications, in which this problem of quantization leads to an error in the position of the peak of correlation (Hearst and Ganapathisubramani 2015). The methods for the detection of the particle centers in PTV are obstructed by this pixel-locking (Feng *et al* 2007). An error based on particle diameter was also observed in OF (Liu *et al* 2020). Intrinsic errors in the resolution of the aperture problem and the dependence on those image flaws have been thoroughly considered (Liu *et al* 2015). These examinations led the community to focus on image-independent spatial constraint or correction methods. A third reason pushed the authors to focus on image-independent constraint and correction. As traditional OF methods minimize the Laplacian of each velocity component, they spatially smooth the calculated velocity field (Seong *et al* 2019). In this sense, it may be questionable to consider the pixel element as the true smallest resolved scale of the optical flow estimate. This is analogous to the fact that the true smallest resolved scale, given by a PIV calculation, does not correspond to the last interrogation window, or a fraction of it if we consider the overlapping (Foucaut *et al* 2004, Nogueira *et al* 2005), although the mathematical arguments are different. As far as the PTV estimate is concerned, every vector is attached to a seeded particle image, i.e., to the true displacement. A lot of work was done, including by the authors, on the derivation of the velocity field from high-density particle images in PTV applications. The idea is to have access to the real motion of each particle, regardless of the quality of the images. Recently, new detection (Cheminet *et al* 2018) and tracking algorithms (Benkovic *et al* 2020) obtained noticeable improvements when applied to images with high particle density. Although a hybridization with PTV has already been proposed for tomographic PIV methods (Novara et al. 2016), this paper aims to develop an optical flow method capable of working at a high density of particles, using the sparse velocity field estimated by PTV as a constraint. However, not all points on the optical flow grid can benefit from this information. There are only velocity vectors attached to the centroids of the detected particles, whereas the OF estimator requires a constraint at each pixel. Consequently, a complementary strategy for the OF constraint is required in the regions where no particles (and their related PTV estimates) are present. Following the arguments mentioned above, it is preferable to design an image-independent optimization based on *a priori* knowledge about the flow.

The remainder of the paper is organized as follows. In Section 2 the proposed algorithm is presented. Section 3 gives details on the design of the test cases. The performance of the proposed algorithm is analyzed in section 4 and compared with a reference OF method. Finally, the main results are synthesized.

2. FBOOF-PTV algorithm

This section introduces a new optimization strategy for optical flow. It is based on the knowledge of sparse velocity fields with sub-pixel accuracy, such as those obtained by PTV, for example. It is designed with the aim to be particularly adapted to the case of highly 3D and unsteady turbulent flows. The context of a high particle density is usually not favorable for PTV (Westerweel *et al* 2013). However, recent detection (Cheminet *et al* 2018) and tracking (Benkovic *et al* 2020) methods have been developed in this context and obtained remarkable results. To apply the new OF method to high particle density images, these new PTV methods are used for this study.

2.1. The tracking-based optimization method

The optimization strategy proposed in this study is based on OF hybridization with PTV. The aim is to benefit from the features of the PTV, i.e. sub-pixel information on a nonstructured mesh embedded with the velocity field estimate. At a given location of the pixel (x, y) in the image, if a particle belongs to its neighborhood (with respect to a user-defined parameter d_c), the velocity of this particle $\mathbf{u_p(t)}$ is used as an anchor for the optimization process. Ideally, if many particles belong to the neighborhood of the considered pixel, a group $V(x, y, t)$ of particles in the neighborhood of the point (x, y) is defined

$$p \in V(x, y, t) \qquad \text{if} \qquad ||\mathbf{x(t)} - \mathbf{x_p(t)}|| < \mathbf{d_c}, \tag{2.1}$$

and a distance-weighted average of the velocities $\mathbf{u_p(t)}$ of all the particles in the neighborhood of the given point (x, y) is performed. The corresponding $\mathbf{\bar{u}_{PTV}(x, y, t)}$ is assigned to the pixel element for the optimization step

$$\mathbf{u_m(x, y, t)} = \mathbf{\bar{u}_{PTV}(x, y, t)}. \tag{2.2}$$

The choice of parameter d_c is intrinsically related to the spatial scales of the velocity field of concern. Ideally, d_c must be kept small enough to ensure that particle motions are coherent in the neighborhood of a given point, that is, a small value of this parameter should be set within the regions of large gradients. Its determination thus requires an *a priori* knowledge of the flow, and a distribution $d_c(x, y)$ can be evaluated by a coarse pre-estimation of the velocity field, either by PIV or OF for example. As the flow of concern here is turbulent, homogeneous, and isotropic, there is no preferential orientation or organization present and we choose to retain $d_c(x, y) = 1$ pixel, which was kept constant for the rest of this study.

The optimization strategy developed in this part is based on the presence of particles together with their PTV estimates in the neighborhood of each pixel of the grid. Since this requirement is not willing to be met, a complementary strategy needs to be proposed in the regions of the image where no particles are found. This is described in the next part.

2.2. The Flow-Based Optimization Optical Flow (FBOOF) method

For computer vision applications, Sun et al. (Sun *et al* 2010) proposed alternatively solving the aperture problem with a median filtering problem. The resolution of the latter was based on *a priori* knowledge of the object displacements embedded in the composition of the image. The proposed method follows this idea: It is derived as a flow-based optimization, that is, it relies on *a priori* knowledge of the flow. After the initial Horn and Schunck (Horn and Schunck 1981) estimation step, one has to resolve the following equations for u and v separately,

$$\begin{cases} \text{minimize} : |\bar{u}(x,y,t) - u(x,y,t)| = 0 \\ \text{constraints} : |\bar{u}(x,y,t) - \tilde{u}(x,y,t)| = 0 \end{cases} \tag{2.3}$$

in which the spatially weighted mean velocity $\bar{u}$ (resp. $\bar{v}$) is defined in the original article by Horn and Schunck (Horn and Schunck 1981) and $\tilde{u}(x,y,t)$ (resp. $\tilde{v}(x,y,t)$) is defined as follows:

$$\tilde{u}(x,y,t) = \frac{\sum_{(x',y')} w_u(x,y,x',y',t)u(x',y',t)}{\sum_{(x',y')} w_u(x,y,x',y',t)} \tag{2.4}$$

$w_u(x,y,x',y',t)$ (resp. $w_v(x,y,x',y',t)$) stands for the weight of the point (x,y) at the instant t calculated from the surrounding points (x',y') as in (2.5).

$$w_u(x,y,x',y',t) = D(x,y,x',y',t) \cdot G_u(x',y',t,u) \cdot W(x',y',t,u,v) \tag{2.5}$$

$$\begin{cases} D(x,y,x',y',t) = e^{-\frac{(x-x')^2+(y-y')^2}{{\sigma_d}^2}} \\ G_u(x',y',t,u) = e^{-\frac{||\nabla \mathbf{u}(\mathbf{x}',\mathbf{y}',\mathbf{t})||^2}{{\sigma_u}^2}} \\ W(x',y',t,u,v) = e^{-\frac{(I(x',y',t)-I(x'-u(x',y',t)dt,y'-v(x',y',t)dt,t+dt))^2}{{\sigma_I}^2}} \end{cases} \tag{2.6}$$

Therefore, at a given point (x,y) in the grid, the evaluated velocity components are modified by the velocity estimates of the surrounding points. A higher weight is given to the closest distant point according to the term $D(x,y,x',y',t)$ as given in (2.5). The term $G_u(x',y',t,u)$ pinpoints the areas of the flow where the gradient velocity field is large, giving less weight in this case. Furthermore, the term $W(x',y',t,u,v)$ in which I corresponds to the intensity of the image identifies the points where the velocity is not the motion between the images. More precisely, the velocity in the current iteration is used to warp (using a cubic interpolation scheme) the image at instant $t+dt$ toward instant t. The differences between the two images could be explained by the lack of convergence of the velocity estimate at this specific point and iteration, or by an inherent error in the image at this point. In any case, this point should have less weight in the optimization process. σ_I only depends on the dynamic range of the gray level in the images. σ_d, σ_u and σ_v are based on the flow. σ_u (resp. σ_v) are directly the spatial average of the flow gradient norms ($\sigma_u = \sqrt{(\frac{\partial u}{\partial x})^2 + (\frac{\partial u}{\partial y})^2}$ and $\sigma_v = \sqrt{(\frac{\partial v}{\partial x})^2 + (\frac{\partial v}{\partial y})^2}$, where the scheme for the derivation of the derivatives uses 5 points), and can be directly estimated using the PIV method. Parameters σ_d, σ_u, σ_v, and σ_I can be evaluated for experimental applications by PIV to find the values that stick the better to the PIV results or by theory to find some known values (inlet flow rate, for example). Using synthetic images, these parameters can be used to find the values that reduce errors.

In order to illustrate how flow-based optimization actually works, Figure 1 shows the four terms D, G_u, G_v and W derived from a synthetic image pair at instants t (Figure 1a) and $t+\Delta t$ (Figure 1d). The flow is uniform: at all points (x, y), the velocity field is $(u, v, w) = (1, 0, 0)$. Therefore, the particle marked by a green circle undergoes an out-of-plane motion between instants t and $t + \Delta t$. G_u (Figure 1b) and G_v (Figure 1e) do not discriminate between the different points due to the gradient-free velocity field. The term D gives more weight to the nearest points (Figure 1c, the point (x, y) in which $D(x, y, x', y', t)$ is located in $(x' = 0, y' = 0)$). Finally, W gives less weight to the pixels attached to the particle that exits the image.

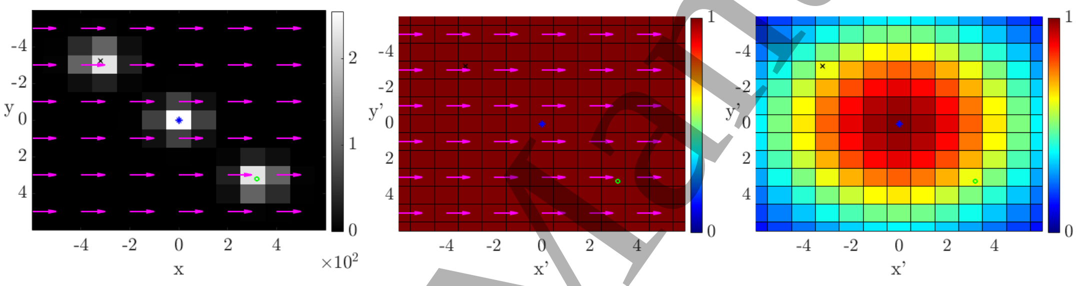

(a) $I(t)$ (b) $G_u(x', y', t, u)$ with $\sigma_u = 1$ (c) $D(x = 0, y = 0, x', y', t)$ with $\sigma_d = 10$

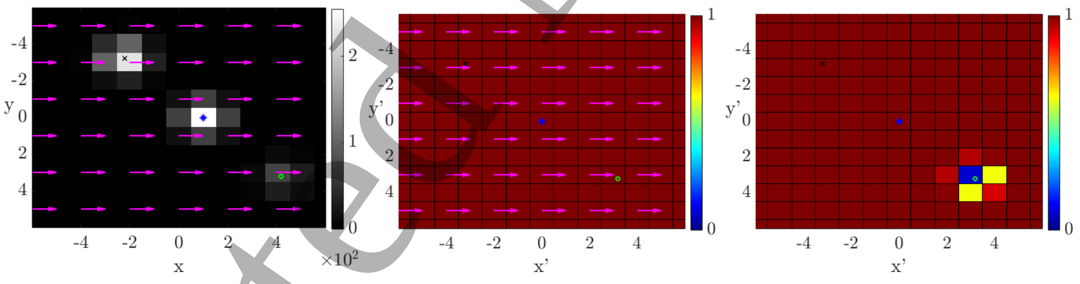

(d) $I(t + \Delta t)$ (e) $G_v(x', y', t, v)$ with $\sigma_v = 1$ (f) $W(x', y', t, u, v)$ with $\sigma_I = 100$

Figure 1: Example of weighted optimization with a pair of images (a) and (d) in which 3 particles (whose centers are represented by a black cross, blue star, and green circle) are subjected to a uniform velocity field. The particle symbolized by the green circle has an out-of-plane motion. The terms D (c), G_u (b), G_v (e), and W (f) are represented.

Figure 2 shows a second illustration. We now consider a single Lamb-Oseen vortex with its core of radius 1 pixel located at $(5, 5)$ and a tangential velocity of 1 pixel superimposed on the uniform flow used in the previous illustration. D is similar to the one in the previous example (Figure 2c) as the nearest pixels have more weight. In contrast, G_u (Figure 2b) and G_v (Figure 2e) allow optimization to discriminate between the flow structures (the vortex ring) by giving less weight to the pixels in a different flow structure. As for W (Figure 2f) is concerned, less weight is given to the pixels subjected to a residual intensity difference once the warping of the image at instant $t + \Delta t$ to the image at instant t with the current velocity estimate has been considered. In this example, this residual is directly related to a quantization error induced by the non-integer local displacement: the smallest weight is attributed to the particle (marked by a green circle) with a displacement close to $(1.5, 1.5)$ pixel in each direction.

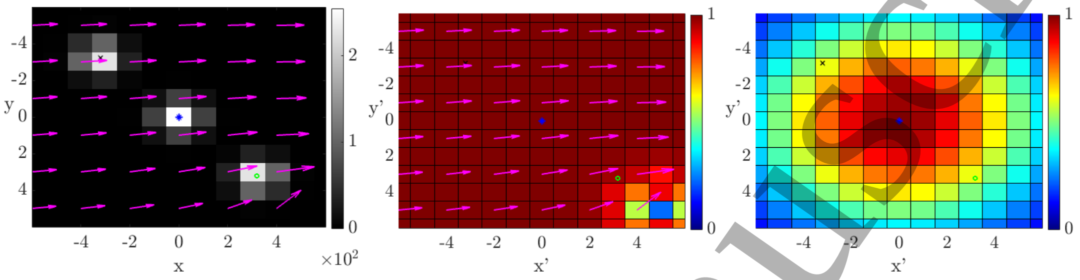

(a) $I(t)$ (b) $G_u(x', y', t, u)$ with $\sigma_u = 1$ (c) $D(x = 0, y = 0, x', y', t)$ with $\sigma_d = 10$

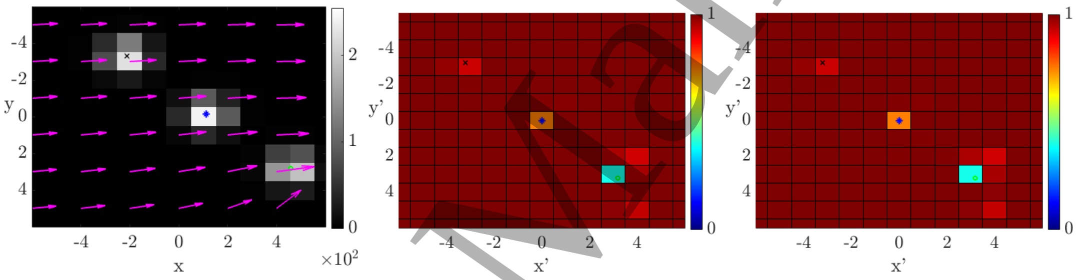

(d) $I(t + \Delta t)$ (e) $G_v(x', y', t, v)$ with $\sigma_v = 1$ (f) $W(x', y', t, u, v)$ with $\sigma_I = 100$

Figure 2: Example of weighted optimization with a pair of two images (a) and (d) in which 3 particles (whose centers are represented by a black cross, blue star, and green circle) are subjected to a uniform velocity field, and to a vortex core on the bottom right of the image. The terms D (c), G_u (b), G_v (e), and W (f) are represented.

In fact, it was shown that resolving (2.3) is equivalent to solving the so-called median problem (Li and Osher 2009):

$$u_m(x, y, t) = \text{median}(\bar{u}, \tilde{u}). \tag{2.7}$$

The two regularization strategies are therefore combined within a single algorithm, as detailed in Algorithm 1. A coarse to fine resolution (Mémin and Pérez 1998) is used to evaluate the "large" displacements. Due to the well-known robustness of these methods, a PIV estimate (using a code available online (Thielicke and Stamhuis 2014)) is used as the initial velocity field at the coarsest pyramidal step. A Gaussian filter of characteristic size σ_{gf} (equal to 2 and 4 pixels for images without and with noise, respectively) is used as a pre-processing step to reduce the noise and illumination changes in the images. The only difference between the two constraints is visible in line 25: If there is a particle in the neighborhood of a given point, u_m is defined as in Equation 2.2, otherwise u_m

is defined as in Equation 2.7. This method is denoted FBOOF-PTV in the rest of the paper.

Algorithm 1: Algorithm of the FBOOF method (the additions for the FBOF-PTV method are shown in red)

```
Result: two-dimensional velocity $\mathbf{u}$=(u,v)
Compute PTV;
Set the residual criterion $\epsilon_{HS}$ (for the Horn and Schunck estimator) and $\epsilon_{FBO}$
  for the Flow-Based Optimization, and the maximum of iterations $iter_{max}$ to
  chosen values;
Set the warping velocity field $(u_w, v_w)$ at $(0, 0)$;
Define the number of pyramidal steps N (for coarse-to-fine resolution);
for k=N to 0 do
    Warp the image at instant $t + dt$ to the one at instant $t$ using $(u_w, v_w)$;
    Compute the two images on the pyramidal grid;
    Compute the derivatives of the image $I_t$, $I_x$ and $I_y$;
    Compute the PIV velocity field $(u_{PIV}, v_{PIV})$;
    Initialize the velocity field $(u, v)$ at $(u_{PIV}, v_{PIV})$;
    Set n to 0;
    # Horn and Schunck estimation;
    while $r > \epsilon_{HS}$ and $n < iter_{max}$ do
        n=n+1;
        Compute $(u^n, v^n)$ as in (Horn and Schunck 1981);
        Compute $r = ||(u^n - u^{n-1}, v^n - v^{n-1})||$;
    end
    Compute $u_w = u_w + u^n$ and $v_w = v_w + v^n$;
    # Flow-Based Optimization;
    Set n to 0;
    while $r > \epsilon_{FBO}$ and $n < iter_{max}$ do
        n=n+1;
        Compute $({w_u}^n, {w_v}^n)$ using (2.5);
        Compute $(\tilde{u}^n, \tilde{v}^n)$ using (2.4);
        Compute ${u_m}^n$ and ${v_m}^n$ using (2.7) and (2.2);
        Compute $r = ||(u_m^n - u_m^{n-1}, v_m^n - v_m^{n-1})||$;
    end
    $u = u_m$ and $v = v_m$;
end
```

3. Tests framework

In this section, we outline the testing framework. We begin with a brief description of the generation of synthetic images and the error metrics used to evaluate the performance of the algorithm. This section ends with a detailed description of the investigated datasets.

3.1. Synthetic images and error metrics

Synthetic images are generated as in Cheminet et al. (Cheminet *et al* 2018). In the images, there is a density of N_{PPP}, expressed in particles per pixel. The mean value of the distances among two neighboring particles d_m usually used for PIV applications will also be provided in this paper (evaluated over the entire image). The positions of the particles are randomly generated and their size is described in the *Point Spread Function* (PSF) model by the size parameter σ_{PSF} (the particle diameter d_p is obtained directly by $d_p = 4\sigma_{PSF}$). To simulate experimental conditions, a Gaussian noise with zero mean and a standard deviation σ_N of 5% is added to each image.

As the theoretical velocity field is known at each pixel, the errors can be derived using the usual RMSE (*Root Mean Square Error*) and AAE (*Average Angular Error*):

$$\begin{cases} RMSE = \sqrt{\dfrac{1}{N}\displaystyle\sum_i ||u_{m_i} - u_{r_i}||^2} \\ AAE = \dfrac{1}{N}\displaystyle\sum_i cos^{-1}\Big(\dfrac{u_{m_i}\cdot u_{r_i}}{||u_{m_i}||||u_{r_i}||}\Big) \end{cases} \tag{3.1}$$

where u_{m_i} (resp. v_{m_i}) is the ith measured vector and u_{r_i} (resp. v_{r_i}) is the ith reference vector.

3.2. Synthetic Lamb-Oseen vortices

The flow constituted of two counter-rotating Lamb-Oseen (LO) vortices (figure 3) is chosen as a test case. The velocity field is derived from an exact solution of the two-dimensional Navier-Stokes equations (in a uniform Cartesian meshgrid):

$$u_\theta = u_{\theta_{max}}\Big(1 + \frac{1}{2\alpha}\Big)\frac{r_0}{r}\Big(1 - e^{-\alpha\frac{r^2}{r_0^2}}\Big) \tag{3.2}$$

where u_θ is the angular velocity component, r is the distance from the center of the vortex, r_0 is the radius of the core (that is, the distance at which the maximum angular velocity is reached), and $\alpha = 1.26$ (Devenport *et al* 1996). An illustration of this steady velocity vector field superimposed onto the curl of this velocity field is shown in figure 3.

The images have $(N_x \times N_y)$ pixel points and the Oseen vortice cores have coordinates (X_1, Y_1) and (X_2, Y_2) (see table 1). A study of the impact of particle density, particle size, and noise is carried out by varying N_{PPP}, σ_{PSF}, and σ_N. Table 1 summarizes the values of all parameters or the range in which they are varied. Statistics are made on 50 image pairs for all $(N_{PPP}, \sigma_{PSF}, \sigma_N)$ considered. To the best of our knowledge, this is

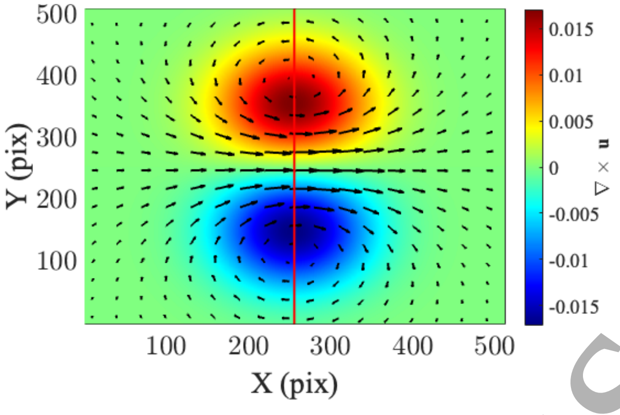

Figure 3: Lamb-Oseen vortex-ring flow: Curl of the velocity superimposed onto the velocity vectors field. The red line is for further comparative analysis.

Table 1: Parameters of the Lamb-Oseen vortex-ring flow test-case.

Parameters	Value or Range
$u_{\theta_{max}}$	2 pixel.s^{-1}
(N_x, N_y)	$(512, 512)$
r_0	$N_x/5$
(X_1, Y_1)	$(N_x/2, N_y/5)$
(X_2, Y_2)	$(N_x/2, 4N_y/5)$
N_{PPP}	$0.04 \rightarrow 0.12$
d_m	$2.51 \rightarrow 1.45$
σ_{PSF}	$0.2 \rightarrow 1.4$
d_p	$0.8 \rightarrow 5.6$
σ_N	0 - 5%

the first time that an OF method has been tested on particle images with a wide range of particle sizes and densities.

3.3. Synthetic images generated from a Turbulent, Homogeneous, and Isotropic flow database

The velocity field used as a reference in this test case comes from a DNS of a THI 3D flow (Li *et al* 2008). This database was already used for the synthetic generation of particle images (Benkovic *et al* 2020, Lee and Hwang 2019). To the author's knowledge, this is, however, the first time that it is used to assess the performances of OF estimates. The velocity fields are extracted at altitudes $z \in [\pi/5 : 9\pi/5]$ from the DNS box, at the instant $t = 2\,\mathrm{s}$, with $(x, y) \in [1.5662, 4.7109]^2$. An illustration of a specific velocity field extracted at $z = \pi/5$ is given in figure 4.

Images of 512×512 pixel size in 8-bit grayscale are generated independently. The size of the pixel is the size of the DNS derivation grid. In each image, the number of particles is specified according to the required particle density, and the locations

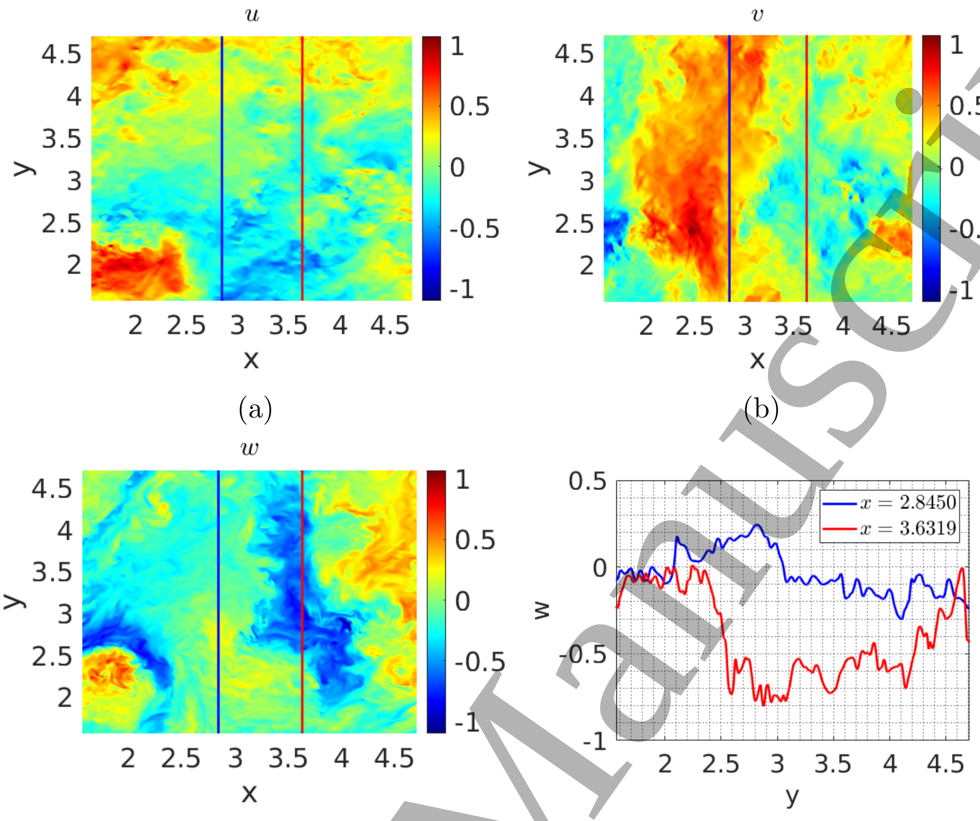

(a) (b) (c) (d)

Figure 4: (a - c): Colormap of the instantaneous velocity components given by the DNS at $z = \pi/5$. (d): Profiles of the third component w along the vertical lines $x = 2.8450$ (blue) and $x = 3.6319$ (red) on which further comparative analysis is conducted.

of the particles are randomly distributed within the entire image. The particles have a diameter of 2.4 pixels, which corresponds to $\sigma_{PSF} = 0.6$. For every image, the associated second frame is determined by estimating the time-delayed particle position with the extracted velocity fields. For this study, we considered 50 pairs of images. The time delay between two images of a single pair is $\Delta t = 5\,\text{ms}$. Those parameters correspond to $\Delta {z_0}^* \approx 2.14$ and $\Delta t^* \approx 0.055$, which are similar to those used previously ($\Delta {z_0}^*$ and Δt^* are the dimensionless laser thickness and inter-frame time defined in table 2 of the paper of Lee and Hwang (Lee and Hwang 2019)).

3.4. Spatial resolution test

The spatial resolution ability of FBOOF-PTV is evaluated with test case A4 of the third international PIV challenge (Stanislas *et al* 2008), which is an open-source PIV test case commonly used to assess whether an algorithm can resolve small spatial scales. This synthetic image pair is a patchwork of four different test cases and comprises flow fields of one- and two-dimensional sinusoids and flow fields that mimic boundary layer flows. We specifically focus on the sinusoidal test cases, which is a one-dimensional sinusoidal shear displacement and is characterized by a varying wavelength in the range of $10 - 400$ pixels. The maximal displacement amplitude varies around 2 pixels. The density of the particles is set to $N_{ppp} = 0.1$.

3.5. Application to a pair of experimental images

Since synthetic images do not model all physical dependencies properly, the ability of FBOOF-PTV to work in a real flow configuration must be evaluated. To this end, we choose an experimental pair of images (available online, (Liu and Salazar 2021)) that is the one used by the reference HOFCC (Liu *et al* 2015). The flow is a jet of air that normally impinges on a black-coated wall. The Reynolds number based on the diameter of the nozzle is $Re = 2600$. More technical information on the experimental setup can be found in (Liu *et al* 2015).

4. Results

We evaluated the new FBOOF-PTV method in different test cases and compared it with a state-of-the-art 2d optical flow algorithm specifically designed for 3d turbulent flows, namely Hybrid Optical-Flow-Cross-Correlation, or HOFCC (Liu *et al* 2020) whose code is available online (Liu and Salazar 2021). HOFCC is a correction of the PIV estimates based on the brightness constancy equation extended to the second order. FBOOF-PTV and HOFCC both use the original Horn and Schunck estimator (HS), so it was also interesting to compare with it. The version used for HS uses a coarse-to-fine strategy and a PIV-based initialization. Similarly, both FBOOF and HOFCC use the PIV method (as initialization for the first one and to warp the images for the second); however, the comparison with PIV was not the purpose of this study. Here all the parameters used are chosen for each method to minimize their errors (the parameters used in the optimization process are available in table 7). The influence of varying particle image diameters, seeding densities, and background noise levels is investigated to evaluate the sensitivity of FBOOF-PTV to these particular effects. Synthetic images are rendered according to section 2.2.

4.1. Results on LO flow

As the FBOOF-PTV method will have to work without PTV estimates in the areas where there are no tracked particles, it is necessary to first validate the FBOOF method alone. This is done specifically in this section, i.e. no PTV estimates are used for the constraint to the brightness constancy equation and only the median problem is considered.

Figure 5 shows the $RMSE$ and AAE errors for the three methods tested on images of particles without noise ($\sigma_N = 0$). Although HOFCC (figures 5b and 5e) is more precise for relatively small particles ($\sigma_{PSF} < 0.4$ pixel), the proposed FBOOF method excels for moderate to large particles, as for the cases of a high particle density (figures 5c and 5f).

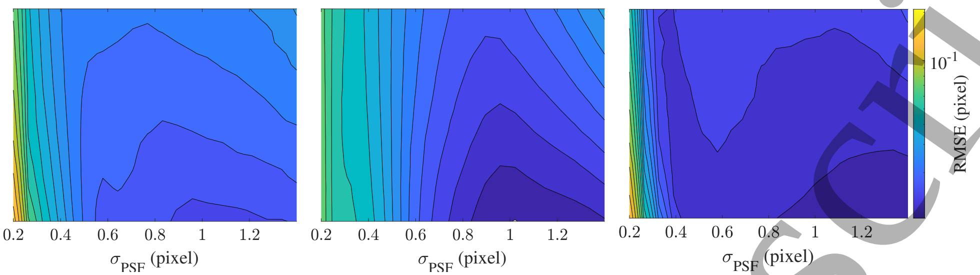

(a) HS (b) HOFCC (c) FBOOF

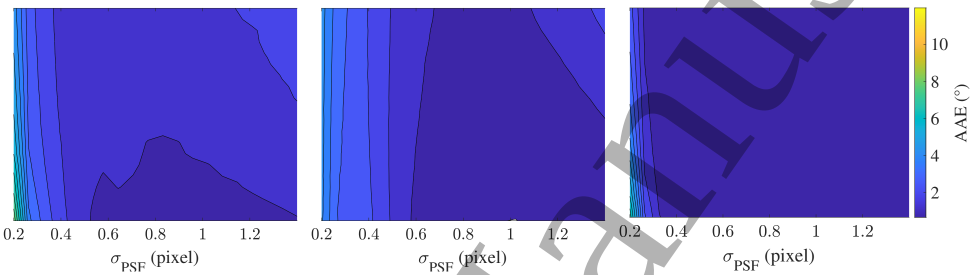

(d) HS (e) HOFCC (f) FBOOF

Figure 5: RMSE (top line) and AAE (bottom line) errors on the velocity norm as obtained by HS, HOFCC, and FBOOF as a function of the particle density (Y-axis) and the particle characteristic size (X-axis). Images without noise.

Table 2 presents the errors of each method tested for a particular case ($\sigma_{PSF} = 0.6$, $N_{PPP} = 0.08$), with and without noise ($\sigma_N = 0$ and $\sigma_N = 0.05$). On images without noise, the superiority of the proposed FBOOF method is clearly visible. For further comparison, the RMSE obtained on laser-induced-fluorescence images by a variational solution of the physics-based Optical Flow (Wang *et al* 2015) was 0.024 pixel for the same flow. The error, in both norm and direction, varies much more with the particle size than with the particle concentration, which is a known result for OF methods (Westerweel 2000). HOFCC obtains better results for moderate particle density and particle size, which confirms previous observations (Liu *et al* 2020). Except for the range of small particles, the results of the current FBOOF method change very little with particle density and particle size compared with the other, which is consistent with the idea of an image-independent correction. One can notice that the FBOOF method is less affected by noise, as its error increases by 20% for RMSE and 29% for AAE, while the errors of the other methods increase between 43% and 70% for the RMSE and between 48% and 78% for the AAE. The FBOOF method seems to be so less dependent on the quality of the images than the others. Self-reliant optimization appears to actually operate as designed.

Figure 6 presents the errors on noisy images. HOFCC no longer obtains better results on relatively small particles (figures 6b and 6e) and approaches the results obtained by HS (figures 6a and 6d). The current FBOOF method obtains better results

Table 2: Errors of the tested methods on the LO test case. Images with, and without noise. $\sigma_{PSF} = 0.6$ pixel ($d_p = 2.4$ pixel) and $N_{PPP} = 0.08$ ($d_m = 1.98$ pixel).

Method	Without noise, $\sigma_N = 0$		With noise, $\sigma_N = 0.05$	
	RMSE (pixel)	AAE (°)	RMSE (pixel)	AAE (°)
HS	0.021	1.375	0.030	2.041
HOFCC	0.020	1.187	0.034	2.113
FBOOF	0.015	0.903	0.018	1.165

than the other methods in all cases, not only with large particles or under conditions of moderate to a high density of particles, but in all the cases tested (figures 6c and 6f).

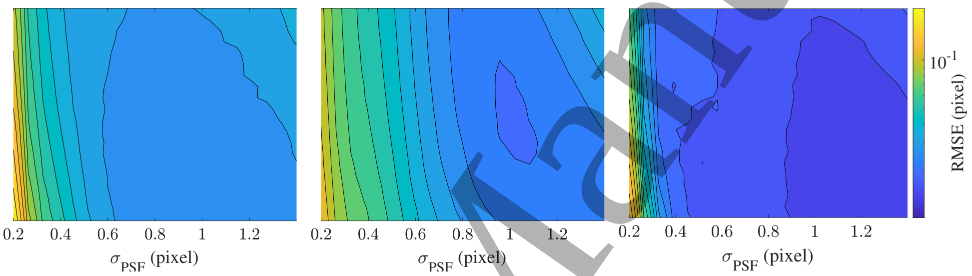

(a) HS (b) HOFCC (c) FBOOF

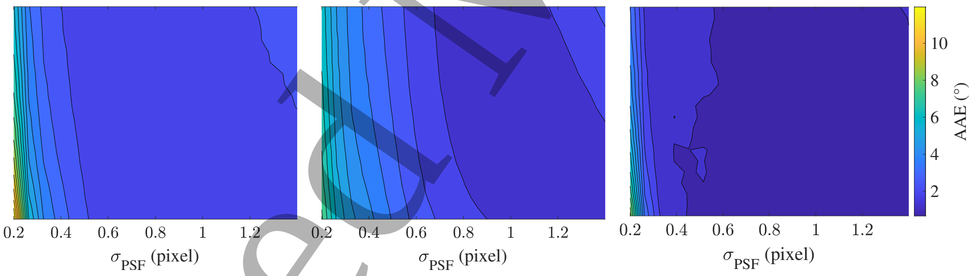

(d) HS (e) HOFCC (f) FBOOF

Figure 6: RMSE (top line) and AAE (bottom line) errors on the velocity norm as obtained by HS, HOFCC, and FBOOF as a function of the particle density (Y-axis) and the particle characteristic size (X-axis). Images with noise.

Figure 7 shows the velocity norm extracted on a line passing by the two cores of the vortex (the red line in figure 3), deduced from each method on the same noisy image pair ($N_{PPP} = 0.08$, $\sigma_{PSF} = 0.6$). It can be seen that FBOOF reconstructs the norm distribution better than any other method, including the variational method in (Wang *et al* 2015). The HS estimator fails to correctly estimate the velocity outside the cores. For all methods, including FBOOF, the area of higher errors coincides with the area of "high" velocity gradients (between or in the two cores, for example).

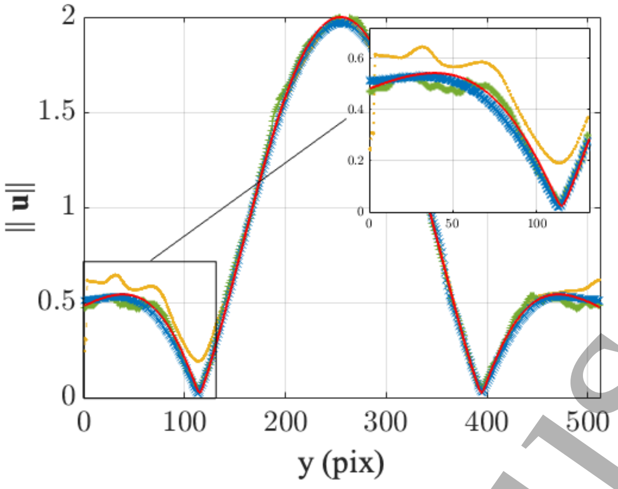

Figure 7: Velocity norm on a line crossing the two vortex cores (see figure 3). Red ——: analytic solution; yellow ······: HS ; green +: HOFCC; blue ×: FBOOF.

4.2. Results on a Turbulent Homogeneous Isotropic 3D (THI3D) flow

The $RMSE$ and AAE errors are estimated at each pixel over 50 pair of images synthesized from 50 different velocity fields at 50 different locations z. All the following results are given in dimensionless units of the DNS (Li *et al* 2008).

The RMSE and AAE errors of the velocity estimates with respect to the particle density N_{PPP} (or the mean value of the distances between neighboring particles d_m in pixel evaluated over all the image) and the measured velocity vector density N_{VPP} (i.e., the density of velocity vectors obtained by PTV) are shown on tables 3 (images without noise) and 4 (noisy images). The difference between each error and the errors of the reference HOFCC (Liu *et al* 2020) is also shown as a percentage. HOFCC is chosen as a reference because it is the most recent method at the time of this study and it was specifically designed for turbulent flows.

Table 3: RMSE and AAE errors as obtained by the tested methods on the THI3D flow test-case. Images without noise.

	$N_{PPP} = 0.06$ $d_m = 2.05$ $N_{VPP} = 0.041$		$N_{PPP} = 0.09$ $d_m = 1.67$ $N_{VPP} = 0.055$		$N_{PPP} = 0.12$ $d_m = 1.45$ $N_{VPP} = 0.063$	
Method	RMSE	AAE (°)	RMSE	AAE (°)	RMSE	AAE (°)
HS	0.111 +31.3%	14.87 +22.4%	0.122 +31.6%	16.19 +21.4%	0.130 +34.2%	17.22 +22.6%
HOFCC	0.084	12.15	0.092	13.34	0.097	14.05
FBOOF-PTV	0.064 -24.2%	9.04 -25.6%	0.069 -25.1%	9.77 -26.8%	0.078 -20.2%	10.91 -22.3%

Table 4: RMSE and AAE errors as obtained by the tested methods on the THI3D flow test case. Images with noise.

	$N_{PPP} = 0.06$ $d_m = 2.05$ $N_{VPP} = 0.039$		$N_{PPP} = 0.09$ $d_m = 1.67$ $N_{VPP} = 0.053$		$N_{PPP} = 0.12$ $d_m = 1.45$ $N_{VPP} = 0.061$	
Method	RMSE	AAE	RMSE	AAE	RMSE	AAE
HS	0.112 +21.2%	15.1 +13.5%	0.122 +24.6%	16.3 +14.8%	0.131 +29.1%	17.3 +17.7%
HOFCC	0.092	13.3	0.098	14.2	0.102	14.7
FBOOF-PTV	0.070 -23.8%	10.0 -24.8%	0.075 -23.4%	10.7 -24.6%	0.082 -19.3%	11.6 -21.1%

The historical Horn-Schunck estimator (Horn and Schunck 1981) does not correctly describe the THI3D flow. HOFCC obtains slightly better results than HS. This implies that the OF correction of this method may not be suitable for this particular kind of flow. Overall, FBOOF-PTV obtains the best results for all particle densities and noise cases. For example, at $N_{PPP} = 0.09$ with noisy images, FBOOF-PTV has errors on the norm and the direction that decrease by 23. 4% and 24. 6%, respectively, with regard to the reference HOFCC.

The global performance criteria, such as those discussed previously, only give a partial insight into the capacity of each method to efficiently estimate the velocity field, particularly for a flow as complex as a THI3D. To better highlight the sensitivity of each method to local flow characteristics, the velocity components u and v are represented in figure 8 along the two vertical lines shown in figure 4: at $x = 2.8450$ over which the third component w has globally minimal amplitude and at $x = 3.6319$ where, in contrast, w presents large amplitudes. Along the latter profile, out-of-plane motions are therefore not to be ignored, which is challenging for estimators limited to a measurement plane. For this comparison, a pair of noisy images at $t = 2\,\mathrm{s}$, $z = \pi/5$ and $N_{PPP} = 0.09$ is considered.

Overall, the tested methods fail to correctly reconstruct the velocity profile with, however, important nuances between them that we want to discuss in the following. When the velocity profiles are of moderate amplitude and exhibit a smooth spatial evolution as observed for $u(x = 2.8450, y)$, the estimates given by all methods are satisfactory. But when the local spatial variations are large as observed for $v(x = 2.8450, y > 2.5)$, large discrepancies appear between the estimates and the true profile given by the DNS.

More importantly, the observed discrepancies between the estimates and the true velocity appear to be closely related to the local amplitude of the third component w (shown in figure 4). Where w significantly deviates from the zero value as observed for $y > 2.4$, the estimates given by HS and HOFCC strongly differ from the reference

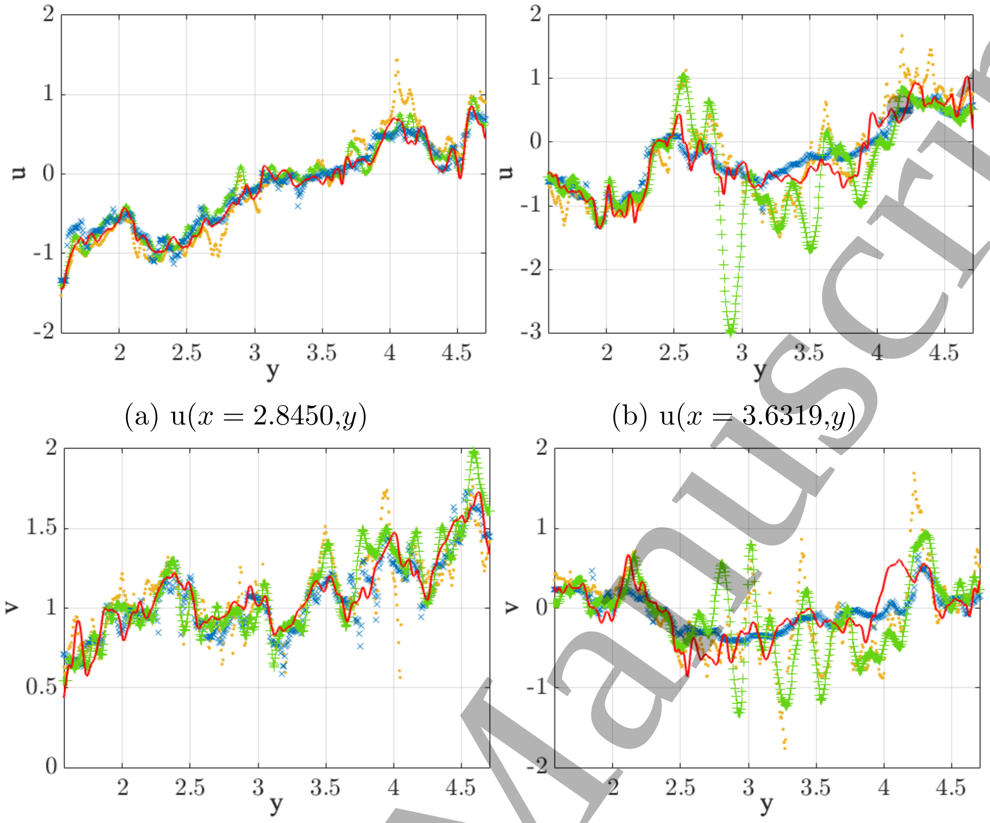

(a) u($x = 2.8450$,y) (b) u($x = 3.6319$,y)

(c) v($x = 2.8450$,y) (d) v($x = 3.6319$,y)

Figure 8: Instantaneous velocity u (top) and v (bottom) components at $x = 2.8450$ (left) and $x = 3.6319$ (right) reconstructed by each method and superimposed onto the original reference DNS (red ——). Yellow ······: HS ; green +: HOFCC; blue ×: FBOOF-PTV. Noisy images with $N_{PPP} = 0.09$.

DNS and tend to overestimate the amplitude of the estimated velocity components in areas where w is large. On the contrary, the velocity estimates computed by FBOOF-PTV tend to smooth out the large local velocity variations and also appear to be less dependent on the third component w than the other methods. The proposed method appears to act as a low-pass filter.

The proposed OF method hybridized with PTV for the optimization process is expected to provide increasing performances with increasing robustness and precision of the PTV method itself and decreasing sparsity of the available information. In this sense, to evaluate the sensitivity of FBOOF-PTV to the PTV estimates, a test is conducted with the same available synthetic database. It consists in computing the FBOOF-PTV velocity fields with the use of the exactly available velocity vectors (given by the DNS) at all trackable particles (which we refer to as ideal PTV) for the optimization process and then comparing it to the previously discussed FBOOF-PTV velocity fields. It should be noted that the density of the velocity vectors (N_{VPP}) increases significantly in comparison with the measured PTV vectors (see table 5). This is especially true

Table 5: Effect PTV robustness and accuracy on the hybridized FBOOF-PTV. Noisy images.

	$N_{PPP} = 0.06$			$N_{PPP} = 0.09$			$N_{PPP} = 0.12$		
Method	N_{VPP}	RMSE	AAE	N_{VPP}	RMSE	AAE	N_{VPP}	RMSE	AAE
FBOOF-PTV (measured PTV)	0.039	0.070	10.0	0.053	0.075	10.7	0.061	0.082	11.6
FBOOF-PTV (ideal PTV)	0.047 +20.5%	0.048 -31.8%	6.98 -30.2%	0.071 +33.4%	0.037 -50.3%	5.46 -50.0%	0.094 +54.1%	0.030 -62.9%	4.50 -61.2%

Table 6: Part τ_{PTV} of optical flow points using PTV information. Noisy images.

	$N_{PPP} = 0.06$		$N_{PPP} = 0.09$		$N_{PPP} = 0.12$	
Method	N_{VPP}	τ_{PTV}	N_{VPP}	τ_{PTV}	N_{VPP}	τ_{PTV}
FBOOF	0	0	0	0	0	0
FBOOF-PTV (measured PTV)	0.039	0.16	0.053	0.21	0.061	0.25
FBOOF-PTV (ideal PTV)	0.047	0.29	0.071	0.40	0.094	0.49

when N_{ppp} is large.

Table 6 shows the rate τ_{PTV} of points in the optical flow grid that are using the PTV information (i.e. the number of pixels verifying Equation 2.1 over the number of total pixels). τ_{PTV} depends on the parameter d_c, which is, in fact, related to the parameter σ_d. In the best case, there are only half of the points that are using the sparse information as an optimization. However, even in the worst case tested in which only 16% of the pixels are using the PTV information, and even with no exact PTV, the FBOOF-PTV method can propagate it and describes the flow with more fidelity than the other tested method.

Figure 9 illustrates a comparison of both instantaneous velocity components determined from FBOOF-PTV using either measured PTV velocity vectors or exact PTV vectors. It is observed that FBOOF-PTV allows for the reconstruction of the instantaneous velocity components, which are quite identical to the reference DNS velocity field. The resulting RMS and AAE errors are indicated in table 5 and are compared to the previous FBOOF-PTV estimates using measured PTV vectors. In this table, the percentage corresponds to the relative difference between both methods. Using ideal PTV velocity vectors, the errors decrease while the density of particles increases. In such an ideal case, it is observed that FBOOF-PTV is able to converge very close to the truth, although the *a priori* information is still very sparse.

4.3. Spatial resolution test

The ability of FBOOF-PTV to accurately resolve even the smallest wavelength is evaluated with test case A4 of the third international PIV challenge (Stanislas *et al*

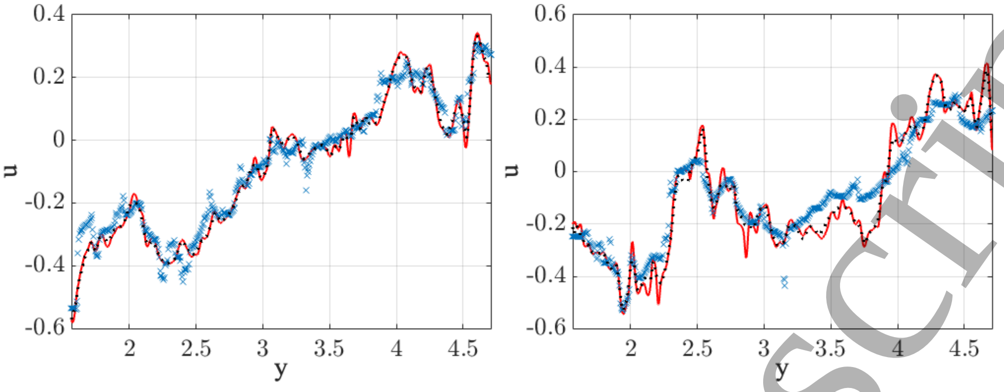

(a) $u(x = 2.8450)$ (b) $u(x = 3.6319)$

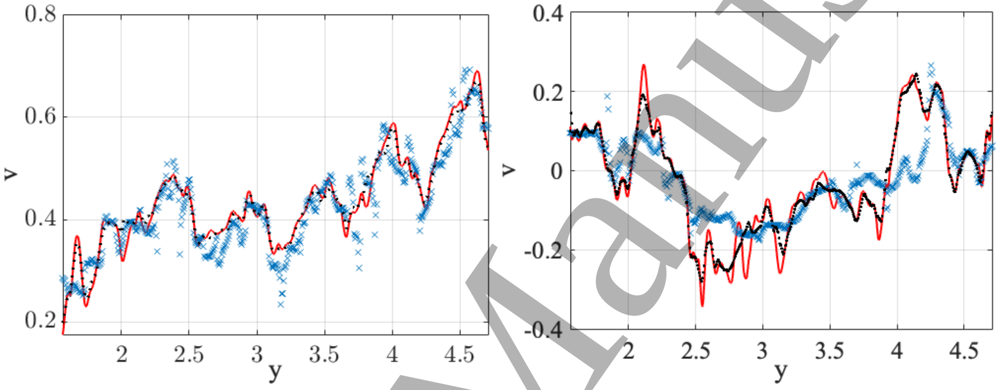

(c) $v(x = 2.8450)$ (d) $v(x = 3.6319)$

Figure 9: Instantaneous velocity u (top) and v (bottom) components at $x = 2.8450$ (left) and $x = 3.6319$ (right) reconstructed by FBOOF-PTV and superimposed onto the original reference DNS (red ——). Black ⋯⋯: true sparse *a priori information* ; blue ×: measured sparse *a priori* information

2008). The particle density is set to $N_{ppp} = 0.1$ and the ratio of unpaired particles is 10%. In this context, our PTV algorithm obtains 30737 vectors with a high level of accuracy (not shown here). The vertical component of the velocity is shown in figure 10 and its average along the vertical direction is presented in figure 11. The top-first and bottom-last ten lines were not considered in the averaging calculation. The ground truth was partly digitized by the authors from Stanislas *et al.* (Stanislas *et al* 2008) to facilitate the analysis. FBOOF-PTV reconstructs the velocity field very precisely and accurately estimates the local displacements even in the range of the lowest wavelengths and very fine spatial scales.

4.4. Application to a pair of experimental images

The parameters used in the optimization process are accessible in table 7. Figure 12 shows the resulting velocity norm obtained by HOFCC (Figure 12a) and FBOOF-PTV (Figure 12b). The close similarity between the two estimates is promising for the robustness of FBOOF-PTV in a real flow configuration, while the efficiency of HOFCC

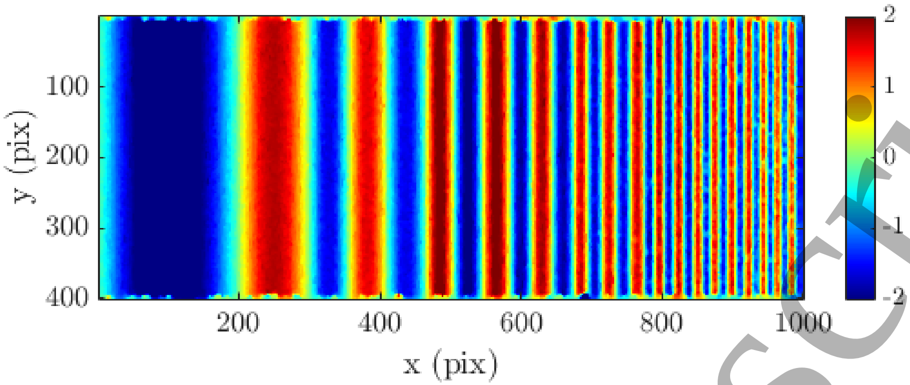

Figure 10: Test case A4 - modulated 1D sine signal. The vertical component of the velocity (in pixel) obtained by FBOOF-PTV.

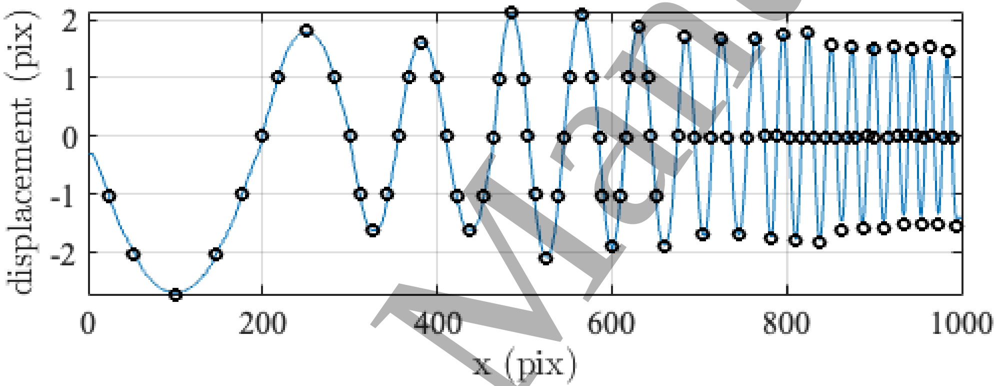

Figure 11: Test case A4 - modulated 1D sine signal. The mean vertical component of the velocity (in pixel) obtained by FBOOF-PTV (blue continuous line) superimposed to the ground truth (black ∘) digitized from (Stanislas *et al* 2008).

on these flows has already been demonstrated (Liu et al. 2020). It should be noted that this image pair is nevertheless the least suitable configuration for FBOOF-PTV due to the poor dynamic range of the images and the low particle density ($N_{PPP} \approx 0.02$, $d_m \approx 2.1$): In case there is no particle in the neighborhood, FBOOF-PTV only resolves the median problem (Equation 2.7) as in the FBOOF method.

5. Conclusion

A new optical flow (OF) estimator was proposed for particle image velocimetry applications. Most current techniques are based on the historical groundwork of computer vision applications. However, it is undoubtedly true that particle images from fluid flow experiments have specificities that are not compatible with the design of an appropriate constraint of the brightness constancy equation, if it were based solely on image features. Therefore, a lot of work has sought to propose a formulation of the constraint independent of the image features. This study was part of this approach. On the basis of recent work by our team, we proposed using Particle Tracking Velocity

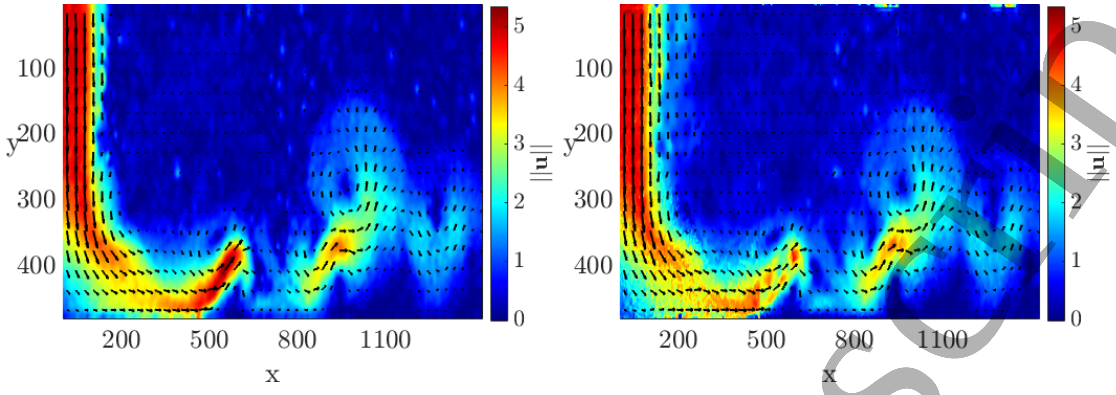

(a) *HOFCC* (b) *FBOOF* – *PTV*

Figure 12: Norm velocity field and velocity vectors of the HOFCC (Liu et al. 2020) on the left and the FBOOF-PTV (on the right) method on an experimental image pair describing an air jet normally impinging a wall.

(PTV) estimates as the constraint to the brightness constancy equation. However, the PTV information remaining sparse in all circumstances (there are only velocity vectors attached to the centroids of the detected particles), so a complementary constraint had to be designed for these regions where no PTV estimate is available. It was built as the median problem based on new image-independent functions. The proposed hybridized method was proposed to be named FBOOF-PTV.

We evaluated the performance of FBOOF-PTV in tens of test cases and revealed its generalization relative to challenging synthetic and experimental PIV images. In particular, we found that FBOOF-PTV is very robust to the range of common error sources (particle density, particle size, and noise) that were tested and exceeds the performance of the gold standard OF algorithm, except for images with particles of relatively small size ($\sigma_{PSF} < 0.4$ pixel). In particular, FBOOF-PTV is well suited for high seeding densities. FBOOF-PTV works accurately for a large range of possible displacements and their respective gradients, while being less sensitive to the out-of-plane component than the reference method. FBOOF-PTV clearly has the potential to resolve small flow structures of large Reynolds number flows. We showed that FBOOF-PTV works reliably under real flow conditions. The predicted flow fields appeared realistic with a detailed representation of small-scale localized features.

More research has to be done with large-scale experimental datasets to demonstrate the ability of FBOOF-PTV to access the small scales of a high Reynolds-number turbulent flow. The sensitivity of the proposed algorithm to out-of-plane motion should also be further studied.

Table 7: Parameters of FBOOF-PTV for each flow. The parameters of the first three flows are estimated by reducing the errors, and those of the last flow are evaluated from PIV estimates.

Flow	Uniform	Lamb-Oseen vortex	THI3D	Modulated sinusoidal test	Wall Jet
σ_d	10	10	0.8	3	1
σ_u	1	10^{-2}	10^{-2}	$\cdot 10^{-1}$	10^{-1}
σ_v	1	10^{-2}	10^{-2}	10^{-3}	10^{-1}
σ_I	100	100	100	500	50

6. Annex

References

Aubert G, Deriche R & Kornprobst P 1999 Computing optical flow via variational techniques *SIAM J. Appl. Math.* **60**(1), 156-182.

Benkovic T, Krawczynski JF & Druault Ph 2020 Vision-based correspondence using relaxation algorithms for particle tracking velocimetry *Meas. Sci. Technol.* **32**(2), 025303.

Cai S, Liang J, Gao Q, Xu C & Wei R 2019 Particle image velocimetry based on a deep learning motion estimator *IEEE Trans. Instrum. Meas.* **69**(6), 3538-3554.

Cheminet A, Krawczynski JF & Druault Ph 2018 Particle image reconstruction for particle detection in particle tracking velocimetry *Meas. Sci. Technol.* **29**(12), 125202.

Chen X, Zillé P, Shao L & Corpetti T 2015 Optical flow for incompressible turbulence motion estimation *Exp. Fluids* **56**(1), 1-14.

Corpetti T, Mémin E & Pérez P 2002 Dense estimation of fluid flows *IEEE Trans. Pattern Anal. Mach. Intell.* **24**(3), 365-380.

Devenport W J, Rife M C, Liapis S I & Follin G J 1996 The structure and development of a wing-tip vortex *J. Fluid Mech.* **312**, 67-106.

Feng Y, Goree J & Liu B 2007 Accurate particle position measurement from images *Rev. Sci. Instrum.* **78**(5), 053704.

Foucaut JM, Carlier J & Stanislas M 2004 PIV optimization for the study of turbulent flow using spectral analysis *Meas. Sci. Technol.* **15**(6), 1046.

Harris J, Smith B L & Wilson B 2012 Investigation of relative importance of some error sources in particle image velocimetry *Fluids Engineering Division Summer Meeting* (ASME) **44762**, 1-11.

Hearst R J & Ganapathisubramani B 2015 Quantification and adjustment of pixel-locking in particle image velocimetry *Exp. Fluids* **56**(10), 1-5.

Heitz D, Héas P, Mémin E & Carlier J 2008 Dynamic consistent correlation-variational approach for robust optical flow estimation *Exp. Fluids* **45**(4), 595-608.

Horn B K & Schunck B G 1981 Determining optical flow *Artif. Intell.* **17**(1), 185-203.

Kadri-Harouna S, Dérian P, Héas P & Mémin E 2013 Divergence-free wavelets and high order regularization *Int. J. Comp. Vis.* **103**(1), 80-99.

Lee H & Hwang W 2019 Error quantification of 3D homogeneous and isotropic turbulence measurements using 2D PIV *Int. J. Heat Fluid Flow* **78**, 108431.

Li Y, Perlman E, Wan M, Yang Y, Burns R, Meneveau C, Burns R, Chen S, Szalay A & Eyink G 2008 A public turbulence database cluster and applications to study Lagrangian evolution of velocity increments in turbulence *J. Turb.* **9**, N31.

Li Y & Osher S 2009 A new median formula with applications to PDE based denoising *Commun. Math. Sci.* **7**(3), 741-753.

Liu T & Shen L 2008 Fluid flow and optical flow *J. Fluid Mech.* **614**, 253-291.

Liu T & Salazar D M 2021 OpenOpticalFlow-PIV: An Open Source Programm Integrating Optical Flow Method with Cross-Correlation Method for Particle Image Velocimetry *J. Open Res. Soft.***9**(1).

Liu T, Merat A, Makhmalbaf M H M, Fajardo C & Merati P 2015 Comparison between optical flow and cross-correlation methods for extraction of velocity fields from particle images *Exp. Fluids* **56**(8), 1-23.

Liu T, Salazar D M , Fagehi H, Ghazwani H, Montefort J & Merati P 2020 Hybrid optical-flow-cross-correlation method for particle image velocimetry *J. Fluids Eng.* **142**(5).

Mémin E & Pérez P 1998 Dense estimation and object-based segmentation of the optical flow with robust techniques *IEEE Trans. Im. Proc.* **7**(5), 703-719.

Novara M, Schanz D, Reuther N, Kähler C and Schröder A 2016 Lagrangian 3D particle tracking in high-speed flows: Shake-The-Box for multi-pulse systems *Exp. Fluids* **57**(8), 1-20.

Nogueira J, Lecuona A & Rodriguez P A 2005 Limits on the resolution of correlation PIV iterative methods. Fundamentals *Exp. Fluids* **39**(2), 305-313.

Schmidt B E & Sutton J A 2019 High-resolution velocimetry from tracer particle fields using a wavelet-based optical flow method *Exp. Fluids* **60**(3), 1-17.

Schneiders J F & Scarano F 2016 Dense velocity reconstruction from tomographic PTV with material derivatives *Exp. Fluids* **57**(9), 1-22.

Schnörr C 1991 Determining optical flow for irregular domains by minimizing quadratic functionals of a certain class *Int. J. Comp. Vis.* **6**(1), 25-38.

Schuster R, Heitz D & Mémin E 2018 Motion estimation under location uncertainty, application to large-scale characterization of a mixing layer *19th Int. Symp. App. Laser Imaging Tech. Fluid Mech.*, 1-20

Seong J H, Song M S, Nunez D, Manera A & Kim E S 2019 Velocity refinement of PIV using global optical flow *Exp. Fluids* **60**(11), 1-13.

Stanislas M, Okamoto, K, Kähler C J, Westerweel J &Scarano F 2007 Main results of the third international PIV challenge *Exp. Fluids* **45**, 27-71

Sun D, Roth S & Black M J 2010 Secrets of optical flow estimation and their principles *IEEE Conf. Comp. Vis. Patt. Recogn.* 2432-2439

Thielicke W & Stamhuis E 2014 PIVlab-towards user-friendly, affordable and accurate digital particle image velocimetry in MATLAB. *J. Open Res. Soft.* **2**(1)

Tikhonov A N, Arsenin V J, Arsenin V I, Arsenin V Y & others 1977 *Solutions of ill-posed problems* (Vh Winston).

Wang B, Cai Z, Shen L & Liu T 2015 An analysis of physics-based optical flow *J. Comput. Appl. Math.* **276**, 62-80.

Westerweel J. 2000 Theoretical analysis of the measurement precision in particle image velocimetry *Exp. Fluids* **29**(1), S003-S012.

Westerweel J, Elsinga G E &Adrian R J 2013 Particle image velocimetry for complex and turbulent flows *Annual Review of Fluid Mechanics* **45**, 409-436